Characterization of Polymer Nanoparticles: An Educational Case Based on PEO–PCL Self-Assemblies Illustrating the Pitfalls to be Avoided

Stéphane Gineste, Alexandre Wodrinski, Tiffany Campion, Pascale Laborie, Jia-Hui Lim, Stéphanie Balor, Barbara Lonetti, Christophe Mingotaud, Jean-Luc Putaux, Anne-Françoise Mingotaud

Characterization of polymer nanoparticles: an educational case based on PEO-PCL self-assemblies illustrating the pitfalls to be avoided

Stéphane Gineste[a], Alexandre Wodrinski[a], Tiffany Campion[a], Pascale Laborie[b], Jia-Hui Lim[c], Stéphanie Balor[d], Barbara Lonetti[a], Christophe Mingotaud[a], Jean-Luc Putaux[c,], Anne-Françoise Mingotaud[a,*]*

[a] Laboratoire Softmat, Université de Toulouse, CNRS UMR 5623, Université Toulouse III – Paul Sabatier, 118 Rte de Narbonne, 31062 Toulouse cedex, France

[b] Institut de Chimie de Toulouse, Université Toulouse 3 Paul Sabatier, ICT-UAR CNRS 2599, 31062 Toulouse France

[c] Univ. Grenoble Alpes, CNRS, CERMAV, F-38000 Grenoble, France

[d] METi, Centre de Biologie Intégrative, Université de Toulouse, CNRS, UPS, 31062, Toulouse, France

*Corresponding authors

Abstract. Although polymer nanoparticles for drug delivery are routinely described, their thorough characterization is often overlooked. Two systems containing self-assemblies of poly(ethylene oxide)-*block*-poly(ε-caprolactone) (PEO-PCL) copolymers are presented to illustrate the extreme caution with which they must be characterized: PEO-PCL 5000-4000 g.mol^{-1} yielded a single

population of micelles, while PEO-PCL 2000-7000 g.mol^{-1} formed a mixture of micelles, vesicles, and wormlike objects. Both were initially characterized by single-angle dynamic light scattering (DLS) and transmission electron microscopy (TEM), as is standard practice. The analysis of the PEO-PCL 5000-4000 micelles demonstrated the relevance of these techniques in such a case. However, while DLS indicated a single population for PEO-PCL 2000-7000, TEM images revealed a mixture of morphologies. Complementary cryo-TEM imaging and multi-angle dynamic and static light scattering analyses provided essential information for an improved characterization. Based on these examples, this article offers recommendations for the reliable characterization of polymer nanoparticles.

Keywords. Polymer, self-assembly, characterization, light scattering, electron microscopy

INTRODUCTION

Over the last thirty years, the benefit of encapsulating drugs into nanoparticles has been clearly established, and the simultaneous progress in polymer engineering has resulted in the multiplication of studies assessing self-assembled polymer nanovectors for applications in oncology or infectiology, for instance.[1-4] Since the aim of such studies was the possible benefit of treating pathologies, the biological result was often shown as the essential one. Unfortunately, this might be associated with the overlooked characterization of the nanovectors themselves. Indeed, a large number of studies cite an early work by Discher and Eisenberg,[5] who described that morphologies could be related to the hydrophilic balance of the copolymer, giving examples of self-assemblies previously predicted.[6] They showed that micelles and polymer vesicles were mainly obtained for hydrophilic balances over 0.45 and below 0.35, respectively, and that wormlike systems were present in between. This rule, demonstrated for specific copolymers in the original

work, has become generally accepted and extended to many types of polymers, although the real situation is more complex, with mixtures of morphologies often present for instance. Furthermore, the lack of thermodynamical control and the kinetic trapping occurring during the copolymer assembly often limited the application of the previous rule and the understanding of the aggregation phenomenon was difficult to generalize. Beyond hydrophilic fraction, from a general standpoint, various publications have underlined the importance of multiple experimental and structural parameters, such as crystallinity or charge, which may influence the resulting morphology.[7-10]

However, the multiplication of studies dealing with nanovectors and the description of seemingly well-established protocols for the formation and characterization of polymer nanovectors would leave researchers thinking that all the associated processes are well-controlled and may be performed quite easily. This might be one of the reasons why comparing biological results between publications is difficult, owing not only to possible differences in biological systems but also to unseen differences in the nanovectors themselves. Indeed, the comparison of self-assembled polymer nanovectors between research teams is difficult. This might come from the polymer (same molar mass, dispersity, or chain ends?) or from the nanovector (same formation protocol, size, or morphology?). Experimental parameters that could be considered as details are known to possibly influence the size or morphology of the formed polymer self-assemblies: speed of the addition in nanoprecipitation procedures, order in the addition of the constituents, stirring speed during the addition, surface state of the support for film rehydration, or the thickness of the film. Another point often limiting comparison between studies is the partial report of results. Indeed, a technique such as dynamic light scattering (DLS) is used as a first-line approach, but publications tend to limit the results to a distribution, either in intensity or only in number, even in some cases without specifying which one is being reported. To improve the rational development

of self-assembled polymer nanovectors for biological applications, a greater attention should be paid to their characterization.

In the course of our work dealing with copolymer nanovectors for photodynamic therapy, we have used poly(ethylene oxide)-*block*-poly(ε-caprolactone) PEO-PCL with a molar mass of 2000-7000 g.mol^{-1} (noted PEO-PCL 2-7) or 5000-4000 g.mol^{-1} (noted PEO-PCL 5-4) amphiphilic copolymers. PEO-PCL copolymers are routinely used in nanomedicine, and we, among others, have published several studies showing that different morphologies formed depending on the polymer and the formation protocol.[7, 11-18] PEO-PCL self-assemblies unsurprisingly exhibited various morphologies depending on the molecular weight of the polymer, the hydrophilic/hydrophobic ratio, or the assembling method. Spherical micelles, vesicles, faceted particles, wormlike micelles, or precipitates have been reported in the literature.[8, 19-22] With a hydrophilic fraction of 0.22 for PEO-PCL 2-7, the rule coming from Eisenberg and Discher suggests that polymer vesicles should be formed in such case. However, we have previously shown that wormlike systems were obtained with this copolymer.[12, 23] Similar results were also published by other teams.[19, 21] In new sets of experiments using these copolymers, we took the opportunity to assess the characterization of their self-assemblies in a slightly different way, only focusing on light scattering and electron microscopy, owing to their easy access. The objective of this work was thus to show how one should be very cautious in analyzing the results using only these two techniques.[24]

EXPERIMENTAL SECTION

Materials. All solvents and chemical compounds besides the copolymers were purchased from Sigma-Aldrich and used without further purification. Water (resistivity 18 MΩ.cm, filtered on a 0.2 µm filter) was obtained from a MilliQ device. Poly(ethylene oxide)-*block*-poly(ε-caprolactone)

2000-7000 and 5000-4000 $g.mol^{-1}$ were purchased from Polymer Source (Dorval, Canada) and used without further purification. Their ^{1}H NMR spectra were in agreement with the molar mass given by the provider (**Figure S1** and **Table S1**). However, the size exclusion chromatography revealed a bimodal distribution for PEO-PCL 2-7 with a mean molar mass M_w = 8400 $g.mol^{-1}$ and M_n = 7300 $g.mol^{-1}$ (**Figure S2** and **Table S1**). PEO-PCL 5-4 micelles were prepared according to previously published procedures,[23, 25] the only modification being the photocrosslinking process described below. This was based on the chain end modification of the PCL block by an acrylate end group which enabled crosslinking.

PEO-PCL 5-4 micelle photocrosslinking. 60 µL of a hexanediol diacrylate 0.12 M solution in acetone and 44 µL of a diphenyl (2,4,6-trimethylbenzoyl)- phosphine oxide (TPO) 2.9 mM solution in acetone were added to a 2-mL solution of acrylate-functionalized PEO-PCL self-assemblies (20 mg of polymer). The solution was degassed under a slow argon flow over 1 h. A 14-mm glass tube containing 2-5 mL of the self-assembly solution was placed at 8 mm between two UV lamps for 2 h (**Figure S3**), Philips linear T5 8W, irradiation at 360 nm, lamp-tube distance 16 mm, total irradiance 17 $mW.cm^{-2}$, measured with an HD9021 photometer from Delta Ohm Inc.

Formation of the PEO-PCL 2-7 self-assemblies. A 20 $mg.mL^{-1}$ PEO-PCL 2-7 solution in chloroform was prepared and the solvent was evaporated on a rotary evaporator to form a regular film that was further vacuum-dried for 4 h. It was then rehydrated with 2 mL of milliQ water, heated at 65 °C for 30 min, and 1 h under sonication at the same temperature. The solution was then extruded on a mini-extruding system from Polar Avanti Lipids with a polycarbonate membrane with a cutoff at 0.4 µm.

Single-angle dynamic light scattering. DLS analyses were carried out at 25 °C on a Malvern (Orsay, France) Zetasizer NanoZS. The solutions were analyzed in triplicate without being filtered in order to characterize the whole sample. Data were analyzed using the general-purpose non-negative least-squares (NNLS) method and the polydispersity index ($PDI_{cumulant}$) obtained through the cumulant method was also recorded. By definition, this PDI is equal to the square of the standard deviation (i.e. the variance) divided by the square of the average of the relaxation rate (see below). The typical accuracy for these measurements was 10-20 % for systems exhibiting a PDI lower than 0.4. All correlograms were further analyzed by the custom-made software M-Storms in order to obtain a more precise characterization of the solutions.[12] This software, designed with Matlab, enables fitting DLS correlograms using different sets of parameters corresponding to all hypotheses to be made during treatment. Indeed, the transition from correlograms to size results implies three steps with different hypotheses: (i) a diffusion coefficient is calculated from the autocorrelation data; (ii) the size of the scattering object is extracted from the diffusion coefficient based on its geometry, (iii) a model is used to convert the intensity-relative population to a number-relative one. For each step, M-Storms provides a choice of different parameters. For the nano-objects described here, the protocol used the NNLS method and the Mie theory, assuming a spherical shape for all objects. In the NNLS calculation, the influence of the regularization parameter α on the distribution is presented below. This parameter affects the narrowness of the distribution peaks by adjusting the regularization.[26] This can be compared to the so-called "general purpose" or "narrow mode" in the Malvern software.

More specifically, M-Storms defines the series of decay rates, Γ_i, following a logarithmic distribution. Then, the sum has to be minimized:

$$\sum_{j=1}^{M}\left(g_j - \sum_{i=1}^{N} a_i . e^{-\Gamma_i . \tau_j}\right)^2$$

where M is the number of experimental points (defined by their index j, their delay times τ_j and the corresponding value of the autocorrelation function, $g_j = g^{(1)}(\tau_j)$, N is the number of classes (i.e. of fixed decay rates), each one being defined by its index i, its decay rates Γ_i and its pre-exponential coefficient a_i. Since these coefficients should be positive, a non-negative constraint is used to solve this problem. This sum can be rewritten in terms of a matrix, which means that one should find the minimum of the Euclidian matrix norm:

$$\|A.x - b\|_2^2$$

where the matrix A contains all the exponential values,

$$\begin{pmatrix} e^{-\Gamma_1 . \tau_1} & \cdots & e^{-\Gamma_1 . \tau_N} \\ \vdots & \ddots & \vdots \\ e^{-\Gamma_M . \tau_1} & \cdots & e^{-\Gamma_M . \tau_N} \end{pmatrix}$$

the x vector contains all the pre-exponential coefficient to be adjusted, $x = \begin{pmatrix} a_1 \\ \vdots \\ a_N \end{pmatrix}$,

and the b vector contains all the autocorrelation values, $b = \begin{pmatrix} g_1 \\ \vdots \\ g_M \end{pmatrix}$.

For the regularization, the second-order Tikhonov regularization matrix RM is defined as:

$$RM = \begin{pmatrix} +1 & -2 & +1 & +0 & \cdots & +0 & +0 & +0 & +0 \\ +0 & +1 & -2 & +1 & \cdots & +0 & +0 & +0 & +0 \\ +0 & +0 & +1 & -2 & \cdots & +0 & +0 & +0 & +0 \\ +0 & +0 & +0 & +1 & \cdots & +0 & +0 & +0 & +0 \\ \vdots & \vdots & \vdots & \vdots & \cdots & \vdots & \vdots & \vdots & \vdots \\ +0 & +0 & +0 & +0 & \cdots & +1 & +0 & +0 & +0 \\ +0 & +0 & +0 & +0 & \cdots & -2 & +1 & +0 & +0 \\ +0 & +0 & +0 & +0 & \cdots & +1 & -2 & +1 & +0 \\ +0 & +0 & +0 & +0 & \cdots & +0 & +1 & -2 & +1 \end{pmatrix}$$

Then the minimization is performed on:

$$\|A.x - b\|_2^2 + \lambda^2.\|RM.x\|_2^2$$

To determine the parameter λ, the Lagrange function equal to $\|A.x - b\|_2^2 + \lambda^2.\|RM.x\|_2^2$ is calculated.[27-28] Its derivative is also estimated and the minimum of this last function is determined. The λ value corresponding to this minimum (multiplied by the regularizer parameter α) is then taken for the NNLS minimization. The software will also estimate a PDI_{NNLS} through the calculation of the mean value and the variance of the relaxation rate distribution obtained from the NNLS minimization.

Multi-angle dynamic light scattering. Multi-angle DLS was used to measure the hydrodynamic radius. Wave scattering vector is described as a function of the angle θ by the equation (1):

$$q = \frac{4\pi n}{\lambda} sin(\theta/2) \qquad (1)$$

where n is the refractive index of the solvent, λ is the wavelength of the incident light. Measurements give access to the autocorrelation function of the scattered light intensity. A mathematical treatment leads to the decay rate Γ, which is related to the diffusion coefficient D_0 ($\Gamma = D_0.q^2$). The hydrodynamic radius is obtained from the Stokes-Einstein relation (Eq. 2),

$$R_h = \frac{kT}{6\pi\eta D_0} \qquad (2)$$

where k is the Boltzmann constant, T is the temperature, and η is the viscosity of the solvent.

Light scattering experiments were performed using a commercial goniometer (3D LS Spectrometer, LS Instruments AG, Switzerland) equipped with a Cobalt laser (λ = 660 nm, 100 mW), a two-channel multiple tau correlator (auto- and crosscorrelation, 1088 real-time channels). The sample cell was held in a decalin-filled quartz vat. The temperature (25 °C) was controlled

using a Julabo CF31 cryo-compact circulator. DLS experiments were carried out from 15 to 150° (corresponding to scattering wave vectors from 2.7×10^{-4} to 2.4×10^{-3} $Å^{-1}$). Typically, measurements were carried out over 30 to 120 s, and at 38 angles selected angles. A 3D setup was used to analyze concentrated samples, which split the beam into two beams, focused in the same spot. Data from scattered light were collected at a specific scattering vector with two independent photon detectors. This configuration eliminated the influence of multiple scattered photons.

Autocorrelation functions were recorded as a function of the scattering angle and the curves were then analyzed with the M-Storms software. For most samples, the resulting distribution of relaxation rates was monomodal. The relaxation rate Γ was linearly q^2-dependent (data not shown), indicating that diffusive motions were probed. The apparent diffusion coefficient D was calculated from the slope of the $\Gamma = f(q^2)$ line. The diffusion coefficient was then used to estimate the hydrodynamic radius (R_H) for the relaxation mode according to the Stokes−Einstein equation. For multimodal distribution, each peak obtained through the NNLS calculation was calculated for all the θ angles and the $\tau = f(q^2)$ relationship led to the average diffusion coefficient associated to the analyzed peak.

Multi-angle static light scattering. The scattering measurements were performed on the same commercial goniometer (3D LS Spectrometer, LS Instruments AG, Switzerland) as for the dynamic measurements. Typically, 10 measurements (5 s each) were collected for 61 selected angles. In MASLS, the excess of scattered intensity by a sample with respect to the solvent is converted into absolute intensity (Rayleigh ratio R_θ, in cm^{-1}) using toluene as a reference (Eq. 3), for which the excess Rayleigh ratio is known ($R_{\theta,toluene}$ = 8.56×10^{-6} cm^{-1} at 660 nm):

$$R_{\theta,sample} = \frac{I_{sample}-I_{solvent}}{I_{toluene}} \cdot \left(\frac{n_{solvent}}{n_{toluene}}\right)^2 \cdot R_{\theta,toluene} \qquad (3)$$

where I_{sample}, $I_{solvent}$, and $I_{toluene}$ are the scattering intensities of the sample solution, the solvent, and the toluene respectively, and where $n_{solvent}$ and $n_{toluene}$ are the refractive indexes of the solvent and the toluene at 660 nm, respectively (n_{water} = 1.33 and $n_{toluene}$= 1.49 at 25 °C).

For particles with a size comparable or smaller than the wavelength of the incident light and with a refractive index close to that of the solvent (Rayleigh−Gans−Debye, RGD, approximation), the Zimm Eq.4 describes the relation between excess of scattered intensity and the parameters of the scattering object:

$$\frac{Kc}{R_\theta} \cong \frac{1}{M_w} \cdot \left(1 + \frac{R_g^2}{3} q^2\right) \cdot (1 + A_2 c) \qquad (4)$$

where c is the concentration, M_w the molecular weight of the scatterers, R_g their radius of gyration, A_2 the second virial coefficient, and K a scattering constant defined as:

$$K = \frac{4\pi^2 n_{solvent}^2}{N_a \lambda^4} \cdot \left(\frac{dn}{dc}\right)^2 \qquad (5)$$

where N_a is the Avogadro number and $\frac{dn}{dc}$ the refractive index increment of the solute. The refractive index increments of the PEO-PCL 2-7 self-assemblies in water were measured with a PSS dndc-2010 instrument at 620 nm at 37 °C and found to be 0.152 mL.g^{-1}. From the partial Zimm plot of $\frac{Kc}{R_\theta}$ *vs* q^2, R_g can be derived from the slope and the intercept $R_g = \left(\frac{3slope}{intercept}\right)^{1/2}$.

The scattered intensity from a particle, as described by the RGD approximation, can be written as:

$$\frac{R_\Theta}{Kc} \propto A\, P(q) \qquad (6)$$

where *A* is an adjusting parameter and *P(q)* is the form factor of the particle and depends on its shape.

In order to describe the data, the SASView software was used for fitting using the following equations for the form factor:[29]

$$P(q) = V\left[\frac{\sin(qr)-qr\cos(qr)}{(qr)^3}\right]^2 \text{ for a sphere of radius r and volume V} \qquad (7)$$

$$P(q) = \int_0^{\pi/2}\left[\frac{\sin(\frac{1}{2}qL\cos\alpha)}{\frac{1}{2}qL\cos\alpha}\,\frac{J_1(qR\sin\alpha)}{qR\sin\alpha}\right]^2 \sin\alpha\, d\alpha \qquad (8)$$

for randomly oriented cylinders with length and radius L and R respectively. J_1 is the first order Bessel function and α the angle between the axis of the cylinder and the scattering vector $\vec{q}$.

For flexible cylinders with length L and Kuhn length b, interested readers can find the detailed equations in the wok by Pedersen et al and Chen et al. [30-31]

$$P(q) = \frac{const}{V_S}\left\{\frac{V_c\,[\sin(qr_c)-qr\cos(qr_c)]}{(qr_c)^3} - \frac{V_T[\sin(qr_T)-qr\cos(qr_T)]}{(qr_T)^3}\right\}^2 \qquad (9)$$

for vesicles with total radius and radius of the core r_T and r_C respectively; total volume V_T, volume of the shell, V_S and volume of the core V_c.

Transmission electron microscopy. Negatively stained specimens were prepared by first depositing droplets of dilute aqueous particle suspensions onto freshly glow-discharged copper grids supporting a carbon film. After 1-3 min, the excess liquid sample was absorbed with filter paper, and before complete drying, a droplet of 1 or 2 wt% uranyl acetate aqueous solution was deposited and left for 2 min. The excess stain was blotted, and the preparations were allowed to air dry. The specimens were observed either with a Jeol JEM-1400 (JEOL Inc, Peabody, MA, USA) at 80 kV with a Gatan Rio9 camera (Gatan Inc, Pleasanton, CA, USA), or a JEOL JEM-2100 Plus microscope operating at 200 kV and equipped with a Gatan Rio16 camera.

Cryo-transmission electron microscopy. Cryo-TEM specimens were prepared by depositing a droplet of particle suspension onto glow-discharged Quantifoil holey carbon grids (Quantifoil Micro Tools GmbH). After absorption of the excess liquid, the specimens were quench-frozen in liquid ethane using a Leica EM-GP workstation, mounted in a Gatan Elsa cryoholder precooled with liquid nitrogen, and transferred into the microscope. All samples were observed with a JEOL JEM-2100 Plus microscope operating at 200 kV and images were recorded with a Gatan Rio 16 camera using the Gatan GMS or SerialEM software.[32] The image analyses were performed using the ImageJ 1.54g software. The size of the different objects was measured manually. For the wormlike systems, the length was estimated manually by approximating the object using multiple segmented lines.

Statistical analyses. Data analysis was performed using GraphPad Prism 8 (GraphPad Software, Inc., La Jolla, CA, USA). Statistical comparisons were performed using t-test if the Fisher test was valid, and Welch's in the opposite case. Overall statistical significance was set at *$p < 0.05$, **$p < 0.01$, ***$p < 0.001$, and ****$p < 0.0001$.

RESULTS AND DISCUSSION

Formation and first-line characterization of the self-assemblies. As previously published, the formation of PEO-PCL 5-4 and PEO-PCL 2-7 self-assemblies is based respectively on a nanoprecipitation method followed by crosslinking and rehydration of a dry film followed by heating, sonication, and extrusion. Such self-assemblies are often characterized by single-angle DLS since the technique is generally readily available.[12, 23] In our case, DLS was performed on a single-angle instrument working at a scattering angle of 173°. The size distribution profiles of both systems show a single population (**Figure 1**). The intensity-averaged and number-averaged

diameters of PEO-PCL 5-4 micelles were 68 and 25 nm, respectively, with a polydispersity index PDI of 0.2. The sizes of PEO-PCL 2-7 assemblies were 210 and 92 nm, respectively, with a PDI of 0.2. Taken as presented, the results appeared consistent, with no evidence of analytical bias.

An additional comment on the PDI must be done here. The PDI mentioned above is $PDI_{cumulant}$ (Γ). PDI(Γ), in DLS, is defined as the ratio of the variance (i.e., the square of the standard deviation) to the square of the mean of the relaxation rate Γ. The radius R of a particle associated to a relaxation rate Γ is proportional to $1/\Gamma$. Therefore, the PDI(Γ) is NOT the PDI(R) and cannot be strictly used to estimate the dispersity in size of the particles. However, if PDI(Γ) is close to zero (i.e. if the Γ distribution is narrow), then PDI(Γ) ≈ PDI(R). If we assume that the distribution of Γ (and therefore R) is relatively narrow, we can estimate R by a Taylor series around the mean value of Γ. This leads to a very rough estimation of PDI(R) (for the distribution in intensity):

$$\mathrm{PDI(R)} \approx \mathrm{PDI}(\Gamma).\left(1 + 2.\mathrm{PDI}(\Gamma) + 3.\mathrm{PDI}(\Gamma)^2 + \cdots\right) \approx \frac{\mathrm{PDI}(\Gamma)}{\left(1-\mathrm{PDI}(\Gamma)\right)^2} \quad \text{for low values of PDI}(\Gamma).$$

(note that the PDI(R) in terms of size distribution in number is different from the PDI(R) of the size distribution in intensity)

A PDI(Γ) below 0.1 is often considered to be the threshold to assert that a size distribution is sufficiently monodisperse in DLS. In this case, the previous formula gives a PDI(R) of *ca*. 0.12. The previous PEO-PCL experimental PDI(Γ) of 0.2 could be associated with a somewhat larger size distribution. In that case, the rough estimation of PDI(R) using the previous formula is 0.31 yielding intensity-averaged sizes of 68 ± 38 nm for PEO-PCL 5-4 and 210 ± 117 nm for PEO-PCL 2-7. This is in agreement with the calculation of the distribution given in **Figure 1B** where the half-height width, i.e. the half-width of the size distribution, is ± 40 nm and ± 130 nm for respectively the PEO-PCL 5-4 and PEO-PCL 2-7.

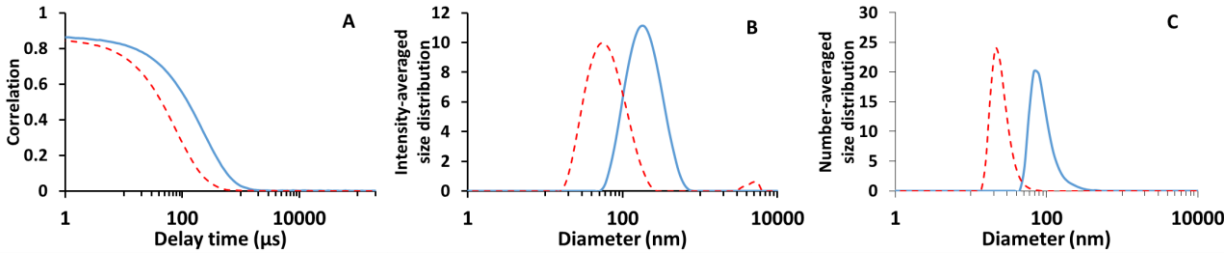

Figure 1. Single-angle DLS analysis of PEO-PCL 5-4 (red dashed line) and 2-7 (blue line) self-assemblies. A) correlograms; B) intensity-averaged size distribution. C: number-averaged size distribution.

Both systems were subsequently observed by TEM. The PEO-PCL 5-4 particles shown in **Figure 2A** were polydisperse spherical micelles. Their size was calculated by considering the diameter of the clear regions outlined by the negative stain. The number-average diameter was 14.1 ± 6.6 nm, with an equivalent PDI_{TEM} (R) of 0.22. The TEM results were consistent with the number-averaged size measured by DLS (25 nm), taking into account a possible deformation of the micelles upon drying on the carbon film and the difficulty in assessing the state of the particle corona, likely swollen in suspension but somewhat contracted in the dry state. Furthermore, these results are consistent with already published results.[15, 19, 33] For systems with a low dispersity, the DLS results can also be compared with the weight-average and Z-average mean sizes calculated from the TEM images and defined as $D_W = \frac{\sum n_i D_i^4}{\sum n_i D_i^3}$ and $D_Z = \frac{\sum n_i D_i^6}{\sum n_i D_i^5}$, respectively, D being the diameter measured directly from the TEM images.[34-35] D_W and D_Z of PEO-PCL 5–4 micelles were 30.0 and 40.0 nm, respectively. They remain quite far from the intensity-averaged size found by DLS at 68 nm, illustrating the significant weight of the largest micelles for light scattering and indicating that that distribution is large with a PDI of 0.2 (**Table 1**). An important point that should be kept in mind is that DLS assesses the size of the scattering object together with the water corona attached to it, by definition, the hydrodynamic size. Furthermore, DLS performs measurements in

the reciprocal space, contrary to TEM working in the direct one. These are other aspects explaining possible differences between DLS and TEM characterization. It is noteworthy that crosslinking did not modify the characteristics of PEO-PCL 5-4 micelles, as demonstrated by DLS data and TEM images collected before crosslinking (**Figure S4**).

The case of PEO-PCL 2-7 assemblies was more complex, since different morphologies were observed by TEM from negatively stained preparations, such as spherical micelles, cylinders, and large spherical objects assumed to be vesicles (**Figure 2B,C**). The internal morphology of the large spherical objects cannot be ascertained by TEM alone and cryo-TEM or scattering techniques should be performed. Spherical micelles and wormlike objects were the major forms (in number). However, the drying of the suspension may have generated artefacts by modifying the particle morphology or promoting particle aggregation. Therefore, cryo-TEM images were also recorded from thin vitreous films of a fast-frozen suspension. A similar variety of morphologies was observed (**Figure 2D,E**), although not in the same apparent proportion. Indeed, while cryo-TEM avoids drying artefacts, others may involve confinement in the holes of the carbon film, as well as a spontaneous size segregation of objects depending on the thickness of the liquid film before freezing.[24, 36-38] Moreover, crystallites of contamination ice could be incorrectly identified as micelles of similar size (**Figure 2E**). The respective concentrations of the suspensions used to prepare negatively stained and fast-frozen specimens should be considered with care since, in the former case, the particles accumulate on the carbon surface, while in the latter, the particles remain within a dilute state in the carbon holes before quenching in liquid ethane. In order to measure comparable numbers of particles from negatively stained and fast-frozen preparations, a rule of thumb is that the suspension concentration for cryo-TEM should be about 100 times higher than that used for negative staining. One should also be cautious when analyzing wormlike systems

since, in crowded regions, long cylinders can superimpose, and detecting both ends of the same objects can be tricky.

For the PEO-PCL 2-7 system, micelles and vesicles with diameters below 40 nm and 50-500 nm, respectively, as well as 100-1700-nm-long wormlike objects were observed in images of either negatively stained or fast-frozen preparations (**Figure 3**). The membrane thickness of the vesicles was *ca.* 20 nm, and the width of the wormlike objects *ca.* 30 nm, within a similar range compared to literature data (**Table 1**).[19, 39]

Table 1. Statistical distribution of the various morphologies observed in TEM images for PEO-PCL 2-7. The fraction of each type of morphology was based on 1414 objects for TEM images of negatively stained preparations and 981 for cryo-TEM images). sd: standard deviation. n: number of objects used for the measurement of size.

	TEM / negative staining			Cryo-TEM		
	Spherical micelles	Vesicles	Cylinders	Spherical micelles	Vesicles	Cylinders
Fraction (% in number)	46	7	47	90	3	7
Average diameter or length (nm) [sd] (*n*)	38.6 [13.5] (*353*)	174 [92] (*104*)	393 [320] (*121*)	30.3 [8.4] (*361*)	153[132] (*43*)	593 [307] (*41*)
Average thickness (nm) [sd] (*n*)	-	27.8 [6.4] (*28*)	36.9 [6.9] (*634*)	-	16.7 [4.4] (*40*)	21.1 [2.9] *(56)*

It must be noted that the dimensions measured from cryo-TEM images were systematically smaller compared to those measured from images of negatively stained preparations. Indeed, several sources of imprecision can be considered in both cases. First, to determine a size distribution, the images were selected depending on the number of discernible objects, which depended on the image magnification and particle size. Having a large number of objects is recommended to improve the counting statistics, but working at low magnification may result in less precise measurements due to the larger defocus that generates more visible Fresnel fringes and

may increase the apparent particle size. This effect is less critical for images of negatively stained preparations since stability and high contrast are provided by the heavy salt stain that outlines the particles. However, it can be more salient in cryo-TEM images since the low electron density of the copolymer particles and the high radiation sensitivity of the ice-embedded specimens limit the accessible magnifications. A compromise should be found between details, contrast, and number of objects, and several images should be analyzed.

Second, choices are made by the observer regarding the way the particle size is measured, in particular, considering that not every region of the particle is properly visible. Indeed, in the case of aqueous suspensions of amphiphilic copolymers, like was the case for the PEO-PCL self-assemblies described in our study, one would expect the spherical micelles and cylinders to be composed of a dense hydrophobic core surrounded by a diffuse corona from the hydrophilic moiety, while the larger vesicles would exhibit a dense membrane with more diffuse layers located on the inner and outer surfaces.[40] In the case of negatively stained particles, it is sometimes difficult to assess the exact location of the contrasting agent that may or may not penetrate, at least partially, the objects. While for solid nanoparticles, the answer is usually assumed to be negative, for copolymer self-assemblies such as those discussed here, the answer is not known with precision, and only assumptions can be made.

As mentioned earlier, after negative staining and drying, the corona can be somewhat retracted and/or partially masked by the accumulated stain. In ice-embedded specimens, one can assume that the corona is still swollen in water before quench-freezing, but it might be invisible in the image due to its low density. Therefore, the observer generally measures the size of the visible regions and underestimate the actual size of the objects. However, indirect effects can be useful in assessing the existence of the corona, in particular when the objects are confined in a region of the specimen but remain at a well-defined interparticle distance. This is illustrated by the images in **Figure 2A**

(negative staining) and **Figure 2E** (cryo-TEM). Assuming that the particles have no surface charge, the repulsion would be of steric nature due to the presence of the diffuse corona, and a correction can be applied to the size of the discernible regions of the particles. In that case, complementary small-angle neutron or X-ray scattering analyses of particle suspensions can be helpful to validate the hypothesis.[33]

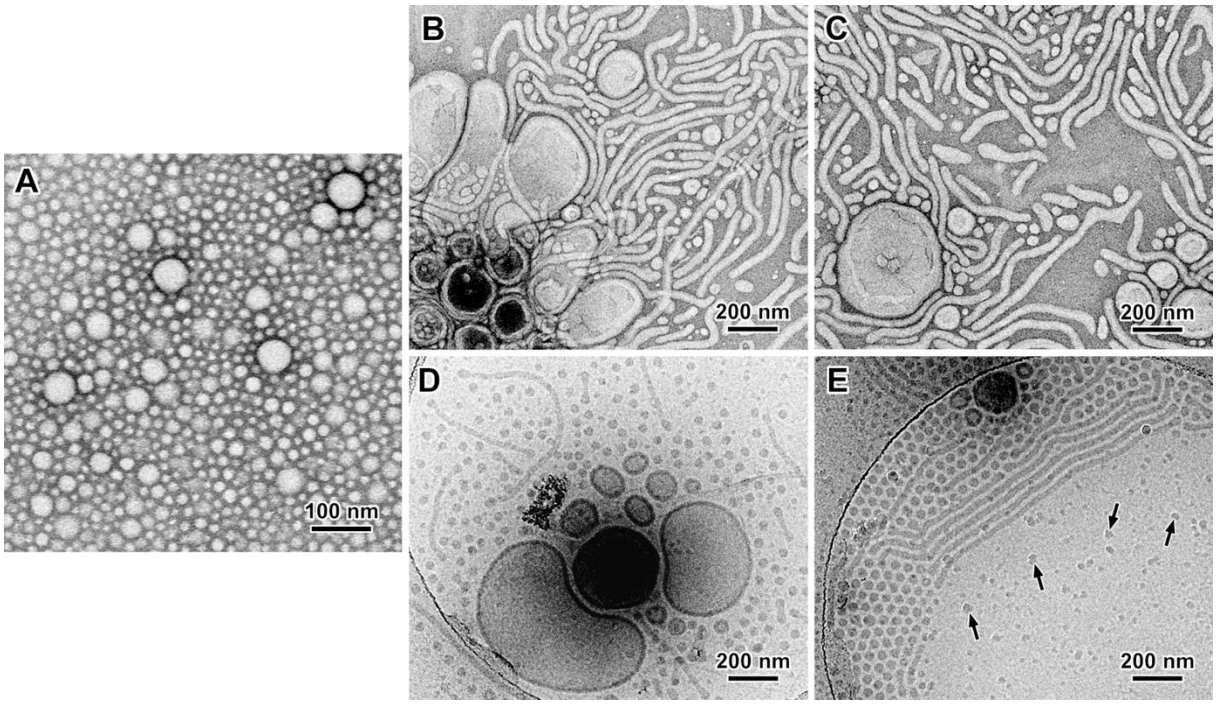

Figure 2. Typical TEM images of PEO-PCL self-assemblies: A) negatively stained preparation of the PEO-PCL 5-4 solution; B,C) negatively stained preparation of the PEO-PCL 2-7 suspension; D,E) fast-frozen film of the PEO-PCL 2-7 suspension. The arrows in E point to a few contamination ice crystallites.

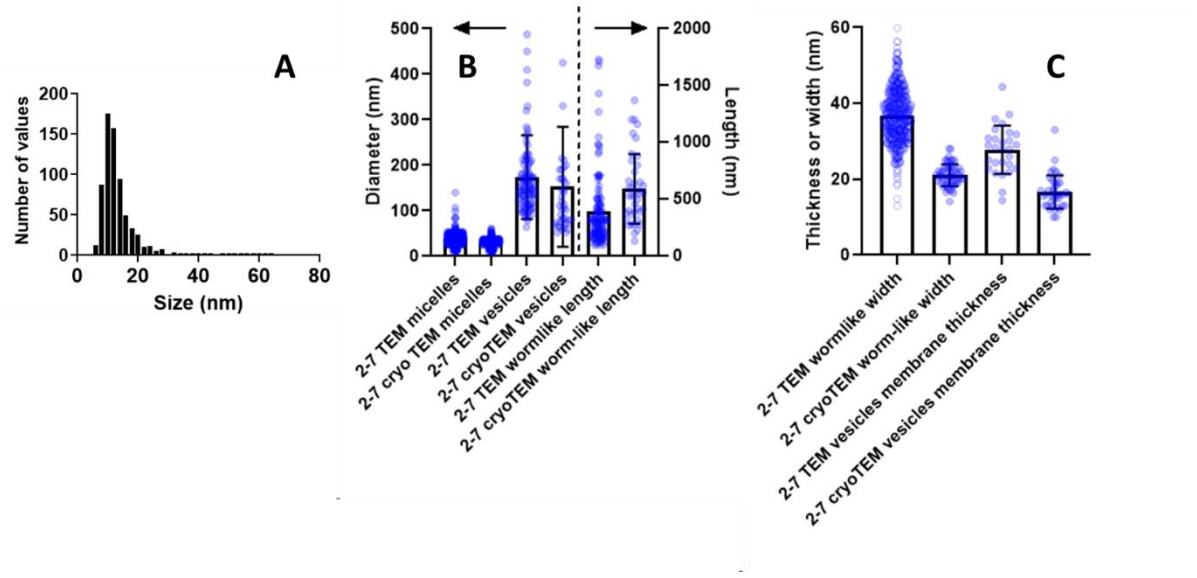

Figure 3. Analysis of TEM images of PEO-PCL self-assemblies: A) size-distribution histogram of PEO-PCL 5-4 micelles; B) corresponding size for each type of PEO-PCL 2-7 self-assembly measured from the TEM images; C) thickness of the vesicle membranes and width of the wormlike objects.

Table 2. DLS results for triplicates of the same PEO-PCL 2-7 suspension analyzed with varying values of the regularizing parameter α in the M-Storms program. For each α value, each line represents one of the triplicate analyses. When two populations were present, the major population was listed first.

α	Intensity-averaged diameter (nm)	Number-averaged diameter (nm)	PDI_{NNLS} (Γ)
1	191 / 32	30	0.8
	195 / 52	50	0.5
	141 / 333	120 / 300	0.1
2	190 / 31	29	0.8
	196 / 54	50	0.4
	144 / 306	113 / 290	0.2
5	188	142 / 254	0.1
	192 / 45	38	0.5
	186	103 / 290	0.2
10	190	128 / 261	0.1
	190 / 34	31	0.5
	185	100 / 280	0.2

TEM images having established that different types of assemblies coexisted in the suspension, could these populations be detected using single-angle DLS? To answer this question, we used the M-Storms software to analyze the DLS results.[12] Starting from the correlograms measured on a single-angle Malvern device, this software enabled assessing different parameter datasets. **Table 2** shows the influence of the α regularizer parameter, which governs the narrowness of the distribution peaks on a PEO-PCL 2-7 suspension. α values of 1 and 10 favor narrow and wide peaks, respectively. The results in **Table 2** were obtained by analyzing triplicates from a single suspension. A clear influence of α was observed, especially on the intensity-averaged distribution, with peaks becoming wider as α increased (**Figure 4A**). The behavior of the number-averaged distribution was even more important and completely erratic, with results switching back and forth, between 30 and 200 nm (**Figure 4B**). Furthermore, comparing the results of the triplicates also showed the extreme sensitivity of the technique. Although the three correlograms could superimpose, as could the fits (**Figure 4C**), the intensity- and number-averaged distributions were significantly different. This behavior may be related to a large size distribution and the presence of several populations. As a comparison, the same changes in parameters have also been applied to the PEO-PCL 5-4 solution (**Figure S5**). The variability was much more limited compared to the PEO-PCL 2-7 system. From these results, it is clear that single-angle DLS by itself cannot be used to characterize several populations separately or to quantify them, and coupling DLS to a separation technique such as flow field-flow fractionation (A4F) is extremely powerful for this.[11-12, 23, 25] However, this goes beyond the scope of this work which primarily aimed at comparing light scattering analysis and electron microscopy data.

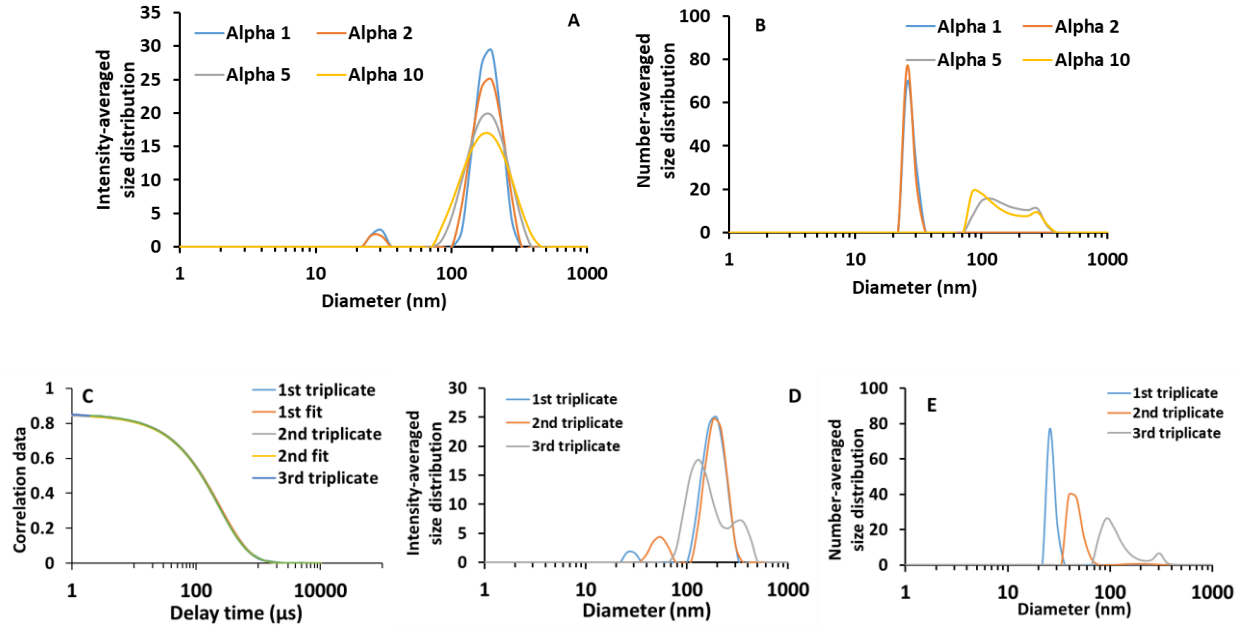

Figure 4. DLS data of PEO-PCL 2-7 analyzed with the M-Storms software. A: Intensity-averaged distribution for a single correlogram at different α values. B: number-averaged distribution for a single correlogram at different α values. C: Correlograms of the triplicates for the considered single solution. D: Intensity-averaged distribution of the triplicates (α = 2). E: Number-averaged distribution of the triplicates (α = 2).

Multi-angle light scattering. The scattering pattern of nano-objects is a function of their size and the measurement at a single scattering angle of 173° introduces a bias by limiting the scattering light coming from larger objects. To assess this limitation, multi-angle DLS and SLS can provide complementary information in the presence of several populations. **Figure 5** shows the correlograms as well as some corresponding fitting curves obtained for a PEO-PCL 2-7 solution at various scattering angles. Different patterns were indeed observed in multi-angle DLS data for PEO-PCL 2-7 self-assemblies, the diameter of the two most important populations being estimated at *ca.* 45 and 200 nm. This experiment confirms the presence of two types of objects with a size of the same order of magnitude as those calculated from the TEM images. The third value (roughly 1700 nm) must be considered with caution since the statistics are poor and the analysis was

performed using the Mie theory for spheres, which is not valid for anisometric objects. It was difficult to assign this peak to wormlike objects or random artefact peaks due to the NNLS calculation.

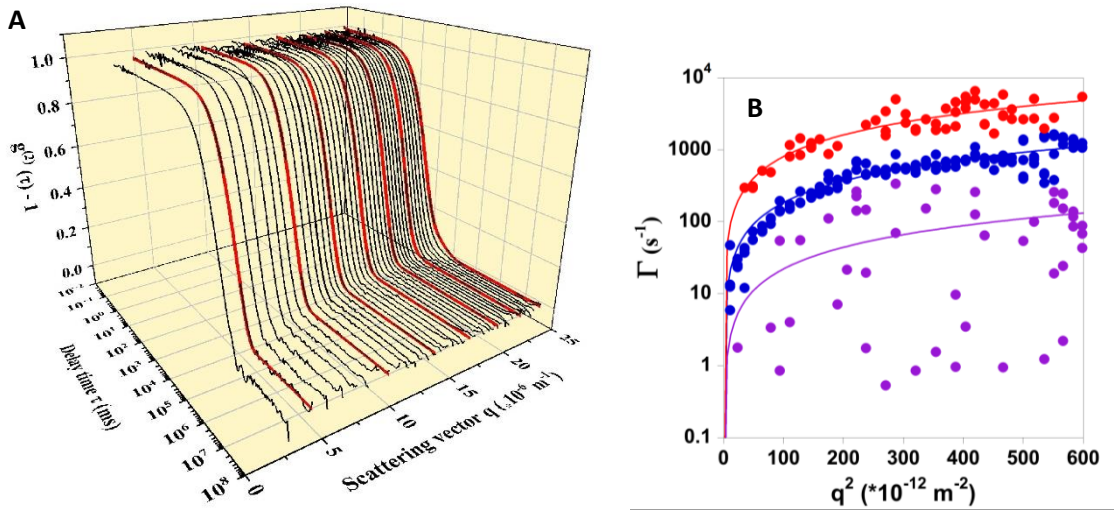

Figure 5. Multi-angle DLS characterization of PEO-PCL 2-7 suspensions. A) 3D representation of correlograms recorded at a scattering angle within the 15-150° range. Examples of fitting curves are drawn in red. B) $\Gamma=f(q^2)$ graph plotting the various populations deduced by NNLS from the correlogram at various angles. The data clouds that correspond to 3 populations of 200, 45 and *ca.* 1700 nm are indicated in blue, red, and purple, respectively. Lines are the linear fit of each set of peaks.

Multi-angle SLS was performed simultaneously to multi-angle DLS and the corresponding data are presented in **Figure 6**. From these SLS data, a mean radius of gyration R_g was deduced either from the Guinier fit or the Zimm plot Kc/R_θ versus q^2 (**Figure S6**). R_g values of 200 or 250 nm, respectively, were obtained, which are intensity-weighted means of R_g of the coexisting self-assemblies. We must underline that these values are a rough estimation due to the interference effect taking place for nanoparticles larger than 100 nm and make the results of Zimm plot less reliable.

In order to assess the shape of the self-assemblies, $\frac{R_\Theta}{Kc}$ was plotted as a function of q and fitted to theoretical equations expressing the form factor $P(q)$ described in the previous section. It must be noted that the experimental data could not be modeled solely as either spheres, or cylindrical objects (**Figure S7**). However, an excellent fit was possible with very polydisperse vesicles by allowing a high background value (4.2×10^6). Due to the available q range, only the diameter value can be trusted (268 ± 102 nm). At this point, without any further information, we can only state that vesicles dominate the scattering profile and that other morphologies are probably present in the sample (indicated by the high background value). Indeed, it is difficult to perform a reliable fit of the data with the sum of two morphologies due to the q-range probed by light scattering and the number of unknown free parameters. In order to have an in-depth characterization, other scattering techniques such as SANS or SAXS would be necessary. These techniques are not always easily available, so we took advantage of the results from cryo-TEM: we implemented the model used for the fitting analysis by allowing a mixture of vesicles, cylinders, and spheres, and used the data obtained from microscopy images in order to decrease the number of free parameters. The width of the vesicle membrane was thus constrained to 20-30 nm. In addition, the radius of the spheres was fixed to 150 nm and the PDI, expressed as σ/R_{mean}, to 0.12 to achieve meaningful results (**Figure 6**) since, within the investigated range, the scattering signal of the small spheres present in the sample corresponded to the constant Guinier regime.

From the fitting results, the cylinder length is estimated to be 1056 nm when no polydispersity is considered, while it decreases to 840 ± 168 nm when assuming a polydispersity index of 0.5 using a Schultz distribution. This enabled the determination of statistically relevant values for the vesicle diameter (280±95 nm) and provided only a rough estimate of the cylinder mean length due to the limited q range and the unknown influence of polydispersity). Comparing the intensity

contributions from vesicles, cylinders, and spheres revealed that the major intensity originated from vesicles (**Figures S8-S10)** where the contribution of each population is shown), despite them being by far the smaller population as revealed by microscopy investigations. It must be noted that the use of a mixture of only vesicles and cylinders also allowed to properly describe the scattering data (**Figure 6**, superimposed black and blue fits).

The light scattering data were accurately interpreted and mean values extracted only by implementing the fits with data from complementary TEM investigations (radius of the small spheres, width of cylinders, and membrane thickness). A larger *q*-range would be required (by using neutron or X-ray experiments, which are not always feasible and often not suited for routine characterization) in order to retrieve information at the corresponding length scale from scattering experiments.

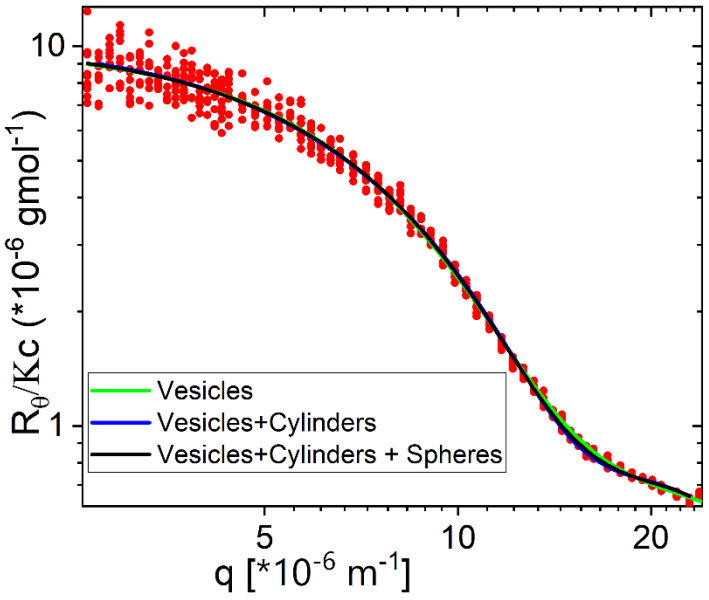

Figure 6. $\frac{R_\Theta}{Kc}$ (symbols) as a function of the scattering vector and corresponding fits (lines) including the contribution of vesicles and cylindrical self-assemblies (blue line) and vesicles, cylindrical self-assemblies and spheres (black line) and vesicles alone (green line).

The aim of this work was to exemplify the difficulties of characterizing polymer nanoparticles suspensions. Possible limitations of our work should be mentioned. The given examples based on PEO-PCL systems are block copolymers, with a possibly crystalline part, and chain end groups which are methoxy and hydroxyl respectively for PEO and PCL. However, the difficulties of analyzing various nanoparticle suspensions will be very close to those described here. Moreover, the copolymer structure given by the provider, is not ideally defined, as shown in supplementary information. PEO-PCL 5-4 molecular weights obtained from SEC and ^{1}H NMR data differ (Mw = 7600 and 8600 g.mol^{-1}, respectively). For PEO-PCL 2-7, SEC data show the presence of a bimodal distribution and the analysis of ^{1}H NMR spectra gives a composition at 1750-6300 g.mol^{-1} and not 2000-7000 as announced by the provider. These flaws are almost always present in studies using commercial or laboratory-synthesized polymers. It is quite rare that the polymers used to form nanoparticles are perfectly defined. The aim of our work was indeed to show some difficulties in this field. Beyond the polymer itself, other difficulties might come from the methodologies used. We have described the difficult interpretation of DLS data and TEM images together with the precautions that should be taken. Another relevant point is which instrument is used. For any technique, one expects that the result should be universal and independent of the instrument. While it is true in a general manner, some variations may occur. An example is provided in supplementary information describing the characterization of two commercial latex solutions by DLS on four different instruments (**Figures S11 and S12**). A last point which is important to underline is the choice of mathematical treatment for the scattering data. In our case, we decided to use Rayleigh theory to analyze SLS data. Since the obtained radii of gyration were larger than 100 nm, the Mie treatment would have been more relevant but went beyond the scope of this article, as only few

analytical solutions are available. Readers who would like deeper information on this can have access to the following references.[41-42]

CONCLUSION

As illustrated by the examples shown in the present paper, one may suggest the following route in order to characterize an unknown solution or suspension of polymer self-assemblies in a trustful manner:

- Single-angle DLS stands as the first readily available technique. Different sets of parameters should be tested, and the results should be considered in a critical manner. If they point to unique values, they can be considered as relevant. The significant modification of the size results by changing a parameter set hints at the presence of several populations. Therefore, the system should be further characterized. Furthermore, correlograms, as well as intensity- and number-averaged analyses, should always be provided when reporting DLS data.
- TEM imaging should also be systematically performed in parallel to single-angle DLS. If both DLS and TEM give similar results (keeping in mind that the size measured from TEM images is usually slightly smaller due to possible drying effects and the sole detection of electron-dense regions of the assemblies) and DLS results are stable with the parameters, the results can be considered as reliable. If TEM and DLS results differ, which can be the case for a significantly polydisperse single population or the existence of multiple populations, a full analysis based on cryo-TEM, multi-angle DLS, and SLS should be performed.

ASSOCIATED CONTENT

Supporting Information. ^{1}H NMR spectra and size exclusion chromatography of PEO-PCL 5-4 and 2-7 copolymers, photocrosslinking set-up, DLS and SLS data treatments. The M-Storms software is available upon request.

AUTHOR INFORMATION

Corresponding Authors

Dr. Anne-Françoise Mingotaud, Laboratoire Softmat, Université de Toulouse, CNRS UMR 5623, Université Toulouse III – Paul Sabatier, 118 Rte de Narbonne, 31062 Toulouse cedex, France, Tel : (33) 561 55 62 72, mail : anne-francoise.mingotaud@cnrs.fr

Dr. Jean-Luc Putaux, Univ. Grenoble Alpes, CNRS, CERMAV, F-38000 Grenoble, France, Tel : (33) 4 76 03 76 04, mail : jean-luc.putaux@cermav.cnrs.fr

Author contribution

Stéphane Gineste, investigation

Alexandre Wodrinski, investigation

Tiffany Campion, investigation

Pascale Laborie, investigation

Jia-Hui Lim, investigation

Stéphanie Balor, investigation

Barbara Lonetti, conceptualization, writing-review and editing

Christophe Mingotaud, conceptualization, writing-review and editing

Jean-Luc Putaux, conceptualization, investigation, writing-original and editing

Anne-Françoise Mingotaud, conceptualization, funding acquisition, supervision, writing-original draft, writing-review and editing

ACKNOWLEDGMENT

We would like to acknowledge the French Research Agency ANR for funding (project TeracellATR ANR-21-CE42-0018) as well as the NanoBio-ICMG Platform (UAR 2607, Grenoble) for granting access to the electron microscopy facility. We also acknowledge the METi imaging facility, a member of the national infrastructure France-BioImaging supported by the French National Research Agency (ANR-10-INBS-04).

REFERENCES

1. Kontogiannis, O.; Selianitis, D.; Lagopati, N.; Pippa, N.; Pispas, S.; Gazouli, M., Surfactant and Block Copolymer Nanostructures: From Design and Development to Nanomedicine Preclinical Studies. *Pharmaceutics* **2023,** *15* (2), 501.

2. Negut, I.; Bita, B., Polymersomes as Innovative, Stimuli-Responsive Platforms for Cancer Therapy. *Pharmaceutics* **2024,** *16* (4), 463.

3. Beach, M. A.; Nayanathara, U.; Gao, Y.; Zhang, C.; Xiong, Y.; Wang, Y.; Such, G. K., Polymeric Nanoparticles for Drug Delivery. *Chem. Rev.* **2024,** *124* (9), 5505-5616.

4. Ghezzi, M.; Pescina, S.; Padula, C.; Santi, P.; Del Favero, E.; Cantù, L.; Nicoli, S., Polymeric Micelles in Drug Delivery: An Insight of the Techniques for their Characterization and Assessment in Biorelevant Conditions. *J. Controlled Release* **2021,** *332*, 312-336.

5. Discher, D. E.; Eisenberg, A., Polymer Vesicles. *Science* **2002,** *297* (9 august 2002), 967-973.

6. Leibler, L.; Orlans, H.; Wheeler, J. C., Theory of critical micelle concentration for solutions of block copolymers. *J. Chem. Phys.* **1983,** *79*, 3550-3557.

7. Dionzou, M.; Morère, A.; Roux, C.; Lonetti, B.; Marty, J.-D.; Mingotaud, C.; Joseph, P.; Goudounèche, D.; Payré, B.; Léonetti, M.; Mingotaud, A. F., Comparison of Methods for the Fabrication and the Characterization of Polymer Self-assemblies: what are the Important Parameters? . *Soft Matter* **2016,** *12*, 2166-2176.

8. Qi, W.; Ghoroghchian, P. P.; Li, G.; Hammer, D. A.; Therien, M. J., Aqueous Self-assembly of Poly(ethylene oxide)-block-poly([varepsilon]-caprolactone) (PEO-b-PCL) Copolymers: Disparate Diblock Copolymer Compositions Give Rise to Nano- and Meso-scale Bilayered Vesicles. *Nanoscale* **2013,** *5* (22), 10908-10915.

9. Crassous, J. J.; Schurtenberger, P.; Ballauff, M.; Mihut, A. M., Design of block copolymer micelles via crystallization. *Polymer* **2015,** *62*, A1-A13.

10. Wright, D. B.; Patterson, J. P.; Pitto-Barry, A.; Cotanda, P.; Chassenieux, C.; Colombani, O.; O'Reilly, R. K., Tuning the aggregation behavior of pH-responsive micelles by copolymerization. *Polym. Chem.* **2015,** *6* (2761-2768).

11. Till, U.; Gaucher-Delmas, M.; Saint-Aguet, P.; Hamon, G.; Marty, J.-D.; Chassenieux, C.; Payré, B.; Goudounèche, D.; Mingotaud, A. F.; Violleau, F., Asymmetrical Flow Field-Flow Fractionation with Multi-Angle Light Scattering and Quasi Elastic Light Scattering for characterization of polymersomes: comparison with classical techniques. *Anal. Bioanal. Chem.* **2014,** *406* (30), 7841-7853.

12. Till, U.; Gibot, L.; Mingotaud, C.; Vicendo, P.; Rols, M. P.; Gaucher, M.; Violleau, F.; Mingotaud, A. F., Self-assembled Polymeric Vectors Mixtures: Characterization of the

Polymorphism and Existence of Synergetic Effects in Photodynamic Therapy. *Nanotechnology* **2016,** *27*, 315102.

13. Geng, Y.; Discher, D., Visualization of Degradable Worm Micelle Breakdown in Relation to Drug Release. *Polymer* **2006,** *47*, 2519-2525.

14. Mikhail, A. S.; Allen, C., Poly(ethylene glycol)-b-poly(ε-caprolactone) Micelles Containing Chemically Conjugated and Physically Entrapped Docetaxel: Synthesis, Characterization, and the Influence of the Drug on Micelle Morphology. *Biomacromolecules* **2010,** *11* (5), 1273-1280.

15. Liu, J.; Zeng, F.; Allen, C., In Vivo Fate of Unimers and Micelles of a Poly(ethylene glycol)-block-poly(caprolactone) Copolymer in Mice Following Intravenous Administration. *Eur. J. Pharm. Biopharm.* **2007,** *65* (3), 309-319.

16. Sachl, R.; Uchman, M.; Matejicek, P.; Prochazka, K.; Stepanek, M.; Spirkova, M., Preparation and Characterization of Self-Assembled Nanoparticles Formed by Poly(ethylene oxide)-block-poly(Îμ-caprolactone) Copolymers with Long Poly(ε-caprolactone) Blocks in Aqueous Solutions. *Langmuir* **2007,** *23* (6), 3395-3400.

17. Sui, X.; Kujala, P.; Janssen, G.-J.; de Jong, E.; Zuhorn, I. S.; van Hest, J. C. M., Robust Formation of Biodegradable Polymersomes by Direct Hydration. *Polym. Chem.* **2015,** *6* (5), 691-696.

18. Jin, S.-M.; Jeon, J.; Park, M.-K.; Kim, G. H.; Lee, E., Multicompartment Vesicles Formation by Emulsification-Induced Assembly of Poly(ethylene oxide)-block-poly(ε-caprolactone) and Their Dual-Loading Capability. *Macromol. Rapid Comm.* **2017**, 1700545-n/a.

19. Du, Z.-X.; Xu, J.-T.; Fan, Z.-Q., Micellar Morphologies of Poly(epsilon caprolactone)-b-poly(ethyleneoxide). *Macromolecules* **2007,** *40*, 7633-7637.

20. Adams, D. J.; Kitchen, C.; Adams, S.; Furzeland, S.; Atkins, D.; Schuetz, P.; Fernyhough, C. M.; Tzokova, N.; Ryan, A. J.; Butler, M. F., On the Mechanism of Formation of Vesicles from Poly(ethylene oxide)-block-poly(caprolactone) Copolymers. *Soft Matter* **2009,** *5* (16), 3086-3096.

21. Du, Z.-X.; Xu, J.-T.; Fan, Z.-Q., Regulation of Micellar Morphology of PCL-b-PEO Block Copolymers by Crystallization Temperature. *Macromol. Rapid Comm.* **2008,** *29* (6), 467-471.

22. Giacomelli, C.; Borsali, R., Morphology of Poly(ethylene oxide)-block-Polycaprolatone Block Copolymer Micelles Controlled via the Preparation Method. *Macromol. Symp.* **2006,** *245-246* (1), 147-153.

23. Till, U.; Gibot, L.; Vicendo, P.; Rols, M. P.; Gaucher, G.; Violleau, F.; Mingotaud, A. F., Crosslinked Polymeric Self-assemblies as an Efficient Strategy for Photodynamic Therapy on 3D Cell Culture. *RSC Advances* **2016,** *6*, 69984-69998.

24. Patterson, J. P.; Robin, M. P.; Chassenieux, C.; Colombani, O.; O'Reilly, R. K., The Analysis of Solution Self-assembled Polymeric Nanomaterials. *Chem. Soc. Rev.* **2014,** *43*, 2412-2425.

25. Gibot, L.; Lemelle, A.; Till, U.; Moukarzel, B.; Mingotaud, A. F.; Pimienta, V.; Saint-Aguet, P.; Rols, M. P.; Gaucher, M.; Violleau, F.; Chassenieux, C.; Vicendo, P., Polymeric Micelles Encapsulating Photosensitizer: Structure/ Photodynamic Therapy Efficiency Relation. *Biomacromolecules* **2014,** *15* (4), 1443-1455.

26. Provencher, S. W., CONTIN: A General Purpose Constrained Regularization Program for Inverting Noisy Linear Algebraic and Integral Equations. *Computer Physics Communications* **1982,** *27* (3), 229-242.

27. Hansen, P. C., Regularization Tools version 4.0 for Matlab 7.3. *Numerical Algorithms* **2007,** *46* (2), 189-194.

28. Hansen, P. C. Regularization Tools: A MATLAB Package for Analysis and Solution of Discrete Ill-Posed Problems. https://www.mathworks.com/matlabcentral/fileexchange/52-regtools?ue

29. https://www.sasview.org/docs/old_docs/5.0.6/ and references therein

30. Pedersen, J. S.; Schurtenberger, P., Scattering Functions of Semiflexible Polymers with and without Excluded Volume Effects. *Macromolecules* **1996,** *29* (23), 7602-7612.

31. Chen, W.-R.; Butler, P. D.; Magid, L. J., Incorporating Intermicellar Interactions in the Fitting of SANS Data from Cationic Wormlike Micelles. *Langmuir* **2006,** *22* (15), 6539-6548.

32. Mastronarde, D. N., SerialEM: A Program for Automated Tilt Series Acquisition on Tecnai Microscopes Using Prediction of Specimen Position. *Microsc. Microanal.* **2003,** *9* (S02), 1182-1183.

33. Till, U.; Gibot, L.; Mingotaud, A.-F.; Ehrhart, J.; Wasungu, L.; Mingotaud, C.; Souchard, J.-P.; Poinso, A.; Rols, M.-P.; Violleau, F.; Vicendo, P. Drug Release by Direct Jump from Poly(ethylene-glycol-b-ε-caprolactone) Nano-Vector to Cell Membrane *Molecules* **2016**, *21*(12), DOI 10.3390/molecules21121643.

34. Putaux, J.-L.; Buléon, A.; Borsali, R.; Chanzy, H., Ultrastructural Aspects of Phytoglycogen from Cryo-transmission Electron Microscopy and Quasi-elastic Light Scattering Data. *Int. J. Biol. Macromol.* **1999,** *26* (2), 145-150.

35. Durrieu, V.; Putaux, J.-L.; Passas, R.; Gandini, A., Cryo-TEM and Image Analysis of Polymer Nanoparticle Dispersions. *Microsc Anal.* **2004,** *18* (1), 19-21.

36. Burrows, N. D.; Penn, R. L., Cryogenic Transmission Electron Microscopy: Aqueous Suspensions of Nanoscale Objects. *Microsc. Microanal.* **2013,** *19* (6), 1542-1553.

37. Koifman, N.; Talmon, Y., Cryogenic Electron Microscopy Methodologies as Analytical Tools for the Study of Self-Assembled Pharmaceutics. *Pharmaceutics* **2021,** *13* (7), 1015.

38. Danino, D., Cryo-TEM of Soft Molecular Assemblies. *Curr. Opin. Colloid Interface Sci.* **2012,** *17* (6), 316-329.

39. Ghoroghchian, P. P.; Li, G.; Levine, D. H.; Davis, K. P.; Bates, F. S.; Hammer, D. A.; Therien, M. J., Bioresorbable Vesicles Formed through Spontaneous Self-Assembly of Amphiphilic Poly(ethylene oxide)-block-polycaprolactone. *Macromolecules* **2006,** *39* (5), 1673-1675.

40. Habel, J.; Ogbonna, A.; Larsen, N.; Cherre, S.; Kynde, S.; Midtgaard, S. R.; Kinoshita, K.; Krabbe, S.; Jensen, G. V.; Hansen, J. S.; Almdal, K.; Helix-Nielsen, C., Selecting analytical tools for characterization of polymersomes in aqueous solution. *RSC Advances* **2015,** *5* (97), 79924-79946.

41. Balderas-Cabrera, C.; Castillo, R., Mie scattering theory applied to light scattering of large nonhomogeneous colloidal spheres. *J. Chem. Phys.* **2024,** *161* (8).

42. Hsieh, A.-H.; Corti, D. S.; Franses, E. I., Rayleigh and Rayleigh-Debye-Gans light scattering intensities and spetroturbidimetry of dispersions of unilamellar vesicles and multilamellar liposomes. *J. Colloid Interface Sci.* **2020,** *578*, 471-483.

For Table of Contents Use Only

Characterization of polymer nanoparticles: an educational case based on PEO-PCL self-assemblies illustrating the pitfalls to be avoided

Stéphane Gineste[a], Alexandre Wodrinski[a], Tiffany Campion[a], Pascale Laborie[b], Jia-Hui Lim[c], Stéphanie Balor[d], Barbara Lonetti[a], Christophe Mingotaud[a], Jean-Luc Putaux[c,], Anne-Françoise Mingotaud[a,*]*